RSC Advances

ROYAL SOCIETY OF CHEMISTRY

PAPER

View Article Online
View Journal | View Issue

Cite this: *RSC Adv.*, 2026, **16**, 20103

Pyrolysis temperature-driven structural evolution of wheat straw biochar and enhanced adsorption mechanisms for Cr(VI)

Jiajia He,† Bo Meng,† Haiyang Qi, Haoyu Fan, Miao Long, Mengjin Yu, Xianming Bao* and Lichao Zhang *

Wheat straw biochars pyrolyzed at 300 °C (WS300) and 500 °C (WS500) were compared for Cr(VI) removal. WS500 exhibited 1.94-fold higher adsorption capacity (23.39 mg g^{-1}) than WS300 (12.07 mg g^{-1}), attributed to its improved pore structure and abundant redox-active groups (*e.g.*, phenolic –OH, C–O–C). Adsorption isotherms followed the Langmuir model, indicating monolayer adsorption. The kinetic process was better described by the pseudo-second-order model, which, together with other analyses, suggests that the adsorption process was likely governed by chemisorption. Integrated characterization (SEM-EDS, BET, XRD, FTIR, XPS) revealed the mechanism: (1) initial rapid uptake *via* surface adsorption and pore filling; (2) Cr(VI) reduction to Cr(III) mediated by phenolic –OH (electron donor) and C–O–C (electron mediators), as evidenced by XPS Cr 2p (Cr(III) at 577.4 eV) and the oxidation of C–OH to O–C=O in C 1s spectra; (3) Cr(III) complexation with oxygen groups, as validated by FTIR Cr–O vibrations (617 cm^{-1}) and XPS Cr(III)–OH signals (532.7 eV). This work clarifies the critical role of pyrolysis temperature in tuning biochar's structure–function relationship for efficient Cr(VI) remediation.

Received 4th January 2026
Accepted 10th April 2026

DOI: 10.1039/d6ra00077k

rsc.li/rsc-advances

1 Introduction

Heavy metals pose significant threats to environmental integrity and human health due to their non-biodegradability and carcinogenic potential.[1,2] Among these, chromium (Cr) is particularly detrimental, as even trace concentrations can induce severe physiological and neurological damage.[3] Chromium naturally exists in two valence states: Cr(III) and Cr(VI). Cr(VI) exhibits potent mutagenicity and teratogenicity and is classified as a group 1 human carcinogen.[4] The World Health Organization has established a strict limit for Cr(VI) in drinking water of 0.05 mg L^{-1}.[3] To address this, various wastewater treatment technologies have been developed, among which adsorption stands out for its efficiency, operational simplicity, cost-effectiveness, and selectivity.[5,6]

Biochar is a carbon-rich material produced by pyrolyzing biomass (*e.g.*, agricultural residues) under oxygen-limited conditions.[7] Owing to its porous structure and abundant oxygen-containing functional groups, biochar has demonstrated considerable potential for remediating heavy metal contamination, particularly chromium.[8,9]

Wheat straw, as one of the most abundant agricultural residues in China, has become a preferred feedstock for biochar preparation due to its wide availability and low cost. Previous studies have confirmed the excellent potential of wheat straw-derived materials for Cr(VI) removal. For instance, Chen *et al.*[6] reported that directly dried wheat straw achieved a saturated Cr(VI) adsorption capacity of 125.6 mg g^{-1} under strongly acidic conditions, attributing this performance to the abundant oxygen-containing functional groups carried by cellulose and hemicellulose in the straw. However, raw wheat straw suffers from poor structural stability in aqueous environments and exhibits a sharp decline in adsorption performance under neutral and weakly acidic conditions, while pyrolysis conversion to biochar can effectively address these limitations while retaining the intrinsic activity of the feedstock. In this context, wheat straw-derived biochar has been increasingly investigated for Cr(VI) removal. Lu *et al.*[10] demonstrated that biochar derived from wheat straw *via* acidic concentrated lithium bromide hydrolysis exhibited a high carbon content and abundant oxygen functional groups, thereby achieving efficient Cr(VI) adsorption. Irfan *et al.*[11] showed that the application of wheat straw biochar to contaminated soil significantly reduced the bioavailability of Cr(VI) and suppressed its uptake by maize plants. Additionally, UV modification has been reported to enhance the adsorption performance of wheat straw biochar.[12] Such treatment increases the specific surface area and introduces additional oxygen-containing functional groups, resulting in a 2–5-fold improvement in Cr(VI) removal capacity compared with unmodified biochar.

To date, the impact of pyrolysis temperature on biochar's Cr(VI) removal performance has been widely documented.

Anhui Province Key Laboratory of Pollutant Sensitive Materials and Environmental Remediation, Huaibei Normal University, Huaibei, 235000, PR China. E-mail: xmbao96@126.com; moerboy6@163.com

† Jiajia He and Bo Meng contributed equally to this paper.

Previous studies have shown that pyrolysis temperature governs the physicochemical properties of biochar, including porous structure and surface functional groups, both of which are known to affect Cr(VI) adsorption.[13,14] However, there remains significant controversy in existing reports: Zuo *et al.*[15] and Zhang *et al.*[16] reported reduced Cr(VI) uptake on corn stover and *L. hexandra* leaf biochars prepared at higher pyrolysis temperatures, whereas Li *et al.*[17] and Singh *et al.*[18] observed enhanced Cr(VI) adsorption on sludge- and *Citrobacter*-derived biochars produced at elevated temperatures. Moreover, the temperature-driven evolution of surface redox-active moieties and the intrinsic mechanism of Cr(VI) sequestration still lack systematic elucidation. Furthermore, most existing studies focus on modified or activated biochar for enhanced Cr(VI) removal. Activation methods including H_3PO_4, KOH, and nano-zero-valent iron (nZVI) can significantly increase the specific surface area of wheat straw biochar, optimize its pore structure, and thus improve its Cr(VI) adsorption capacity.[19–21] However, such post-pyrolysis treatments inevitably introduce confounding factors, including altered pore structures and artificially introduced active sites, which obscure the inherent effect of pyrolysis temperature on the intrinsic surface redox behavior of biochar.

Herein, we investigated Cr(VI) adsorption on wheat straw biochars pyrolyzed at 300 °C (WS300) and 500 °C (WS500) without any modification. This experimental design could effectively isolate the intrinsic effect of pyrolysis temperature and avoid the interference of additional treatment processes on the physicochemical properties of biochar. Multiple analytical techniques, including elemental analysis, thermogravimetric analysis (TGA), Brunauer–Emmett–Teller (BET) specific surface area analysis, scanning electron microscopy with energy-dispersive X-ray spectroscopy (SEM-EDS), Fourier transform infrared spectroscopy (FTIR), X-ray diffraction (XRD), and X-ray photoelectron spectroscopy (XPS), were employed to characterize the physicochemical properties of the biochars prepared at different pyrolysis temperatures. Batch adsorption experiments were conducted to compare the Cr(VI) removal performance of the as-prepared biochars. The primary objective of this work was to elucidate the fundamental evolution of biochar surface redox chemistry driven by pyrolysis temperature, establish the structure–activity relationship among pyrolysis temperature, surface redox characteristics, and Cr(VI) removal performance of biochar, and reveal the underlying mechanism of pyrolysis temperature-regulated Cr(VI) removal by biochar.

2 Materials and methods

2.1 Materials and reagents

Wheat straw was collected from agricultural fields in Huaibei City, Anhui Province, China. The straw was thoroughly rinsed with deionized water, air-dried in sunlight, and then further dried in an oven at 80 °C. The dried wheat straw was pulverized using a laboratory mill, passed through a 2 mm sieve, and stored in sealed containers until further use.

Biochars were synthesized *via* oxygen-limited pyrolysis of wheat straw in a muffle furnace under N_2 atmosphere (flow rate: 200 mL min^{-1}). Pyrolysis was conducted at 300 °C and 500 °C for 2 h with a heating rate of 10 °C min^{-1}. After pyrolysis, the samples were cooled to ambient temperature and collected. The obtained products were ground using an agate mortar and pestle, sieved through a 100-mesh sieve, and sealed in airtight bags for subsequent use. The biochars prepared at different pyrolysis temperatures were designated as WS300 and WS500, respectively. Potassium dichromate ($K_2Cr_2O_7$, analytical grade, ≥99.8%) was used as the Cr(VI) source.

2.2 Characterization of biochar

The bulk elemental contents of carbon (C), hydrogen (H), nitrogen (N), and sulfur (S) in the biochars were determined using an elemental analyzer (Vario EL Cube, Elementar, Germany). Oxygen (O) content was calculated *via* mass balance. The thermal stability of wheat straw was measured using a simultaneous thermal analyzer under N_2 atmosphere at a heating rate of 10 °C min^{-1} from room temperature to 800 °C (STA200, Hitachi, Japan). Specific surface area and pore volume were determined by N_2 physisorption at −196 °C (ASAP 2460, Micromeritics, USA; degassing under vacuum at 60 °C for 3 h). Micromorphology and elemental mapping were examined by SEM-EDS (Regulus 8220, Hitachi, Japan). Crystalline phases were analyzed by XRD (Empyrean, Malvern Panalytical, Netherlands; Cu-Kα radiation, 40 kV, 40 mA, 2θ range: 5–80°). Surface functional groups were characterized by FTIR (Nicolet iS50, Thermo Fisher, USA; KBr pellet method, 400–4000 cm^{-1}). Surface elemental composition and chemical states were analyzed by XPS (Axis Supra+, Kratos, Japan; monochromatic Al-Kα source, 1486.69 eV, 150 W, vacuum level: 5×10^{-9} torr, binding energy range: 0–1200 eV for survey spectra, full-spectrum scans: 1, narrow-region scans: 1–5 depending on signal strength). XPS spectra were processed using CasaXPS (v2.3.24) with charge correction to C 1s at 284.8 eV.

2.3 Adsorption experiments

For isothermal adsorption experiments, 0.100 g of biochar was added to a 50 mL centrifuge tube containing 30 mL of Cr(VI) solution (prepared from $K_2Cr_2O_7$). The initial solution pH was adjusted to 6.0 using 0.1 M HCl or NaOH, as this value falls within the typical pH range of natural waters (6.0–8.0)[22] and avoids both the instability of biochar under strongly acidic conditions and the potential precipitation of chromium hydroxides under alkaline conditions,[23] thereby allowing a focused investigation of the adsorption process. Initial Cr(VI) concentrations ranged from 1 to 300 mg L^{-1} (1, 20, 40, 60, 80, 100, 120, 150, 200, 300 mg L^{-1}). Biochar-free controls were included to quantify non-adsorptive losses. Tubes were shaken (120 rpm, 25 ± 0.5 °C) for 24 h (equilibrium confirmed by preliminary tests). Solutions were then filtered (0.45 μm PTFE membrane), and Cr(VI) concentrations in the filtrate were measured using the diphenylcarbazide (DPCI) method.[24] The detailed procedure, including reagent preparation and colorimetric determination, is provided in the SI (SI. 1). To determine total chromium, an aliquot of the filtrate was subjected to oxidation using potassium permanganate ($KMnO_4$) in an acidic medium, followed by the same DPCI method analysis. The

concentration of Cr(III) was calculated as the difference between total Cr and Cr(VI). The biochar from the 200 mg L^{-1} adsorption group was rapidly rinsed with deionized water until the Cr(VI) concentration in the rinse solution fell below the detection limit, and then freeze-dried (−50 °C, 48 h) for post-adsorption characterization.

For kinetic adsorption experiments, a total of 0.100 g biochar was mixed with 30 mL Cr(VI) solution (80 mg L^{-1}, pH 6.0) in 50 mL tubes. Triplicate samples were shaken (120 rpm, 25 ± 0.5 °C), and aliquots were collected at t = 1, 5, 10, 15, 30, 60, 120, 240, 480, 960, 1440 min. Solutions were filtered (0.45 μm PTFE), and Cr(VI) concentrations were analyzed as above. Biochar-free controls were processed identically.

2.4 Data processing

The Langmuir and Freundlich isotherm models were applied to fit the data, with model fitting and data plotting conducted through Origin 2021 software. Eqn (1) and (2) represent these two models, respectively.

$$q_e = C_e \times q_m \times K_L/(1 + K_L \times C_e) \quad (1)$$

$$q_e = K_f \times C_e^{1/n} \quad (2)$$

where C_e represents the equilibrium concentration of Cr(VI) (mg L^{-1}), q_m denotes the theoretical maximum adsorption capacity according to the Langmuir model (mg g^{-1}), K_L is the Langmuir constant (L mg^{-1}), q_e is the adsorption capacity of the adsorbent at equilibrium (mg g^{-1}), K_f is the Freundlich constant ((mg g^{-1})((mg L^{-1})$^{-1}$)$^{1/n}$), and n is a Freundlich constant indicative of heterogeneity and adsorption intensity.

The kinetics adsorption experimental results were analyzed using both the pseudo-first-order (PFO) kinetic model (eqn (3)) and the pseudo-second-order (PSO) kinetic model (eqn (4)). The rate-limiting step of the adsorption process was assessed using the intraparticle diffusion model (eqn (5)):

$$q_t = q_e - \exp(\ln(q_e) - K_1 t) \quad (3)$$

$$t/q_t = 1/K_2 q_e^2 + t/q_e \quad (4)$$

$$q_t = K_d t^{1/2} + C \quad (5)$$

where q_t (mg g^{-1}) represents the adsorption capacity at any given time t (min); q_e (mg g^{-1}) represents the equilibrium adsorption capacity; K_1 (min^{-1}) and K_2 (g (mg min)$^{-1}$) are the equilibrium rate constants; K_d (g (mg $min^{1/2}$)$^{-1}$) is the internal diffusion rate constant; and C is a constant related to boundary layer thickness.

3 Results and discussion

3.1 Adsorption isotherm

Fig. 1 depicts the adsorption isotherms of Cr(VI) onto WS300 and WS500. It illustrates that as the concentration of Cr(VI) increases, the equilibrium adsorption capacity of both biochars progressively rises. When the initial concentration reached 200 mg L^{-1}, the adsorption process approached saturation, evinced by the gradual leveling off of the curve. At lower concentrations, unoccupied sites facilitate increased adsorption; additionally, higher concentrations intensify mass transfer driving forces.[25] However, saturation occurs as sites become fully occupied.

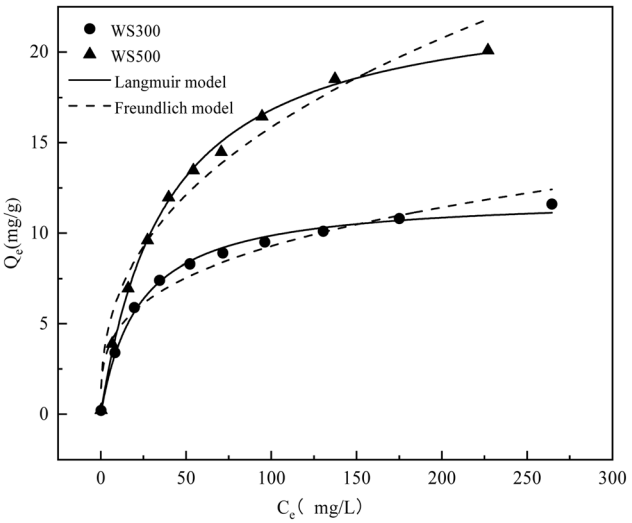

Fig. 1 Adsorption isotherms of Cr(VI) onto WS300 and WS500. The solid lines represent the Langmuir model fitting curves, whereas the dashed lines represent the Freundlich model fitting curves.

According to Table 1, the saturated adsorption capacities were 12.07 mg g^{-1} (WS300) and 23.39 mg g^{-1} (WS500), confirming a 1.94-fold higher capacity for WS500. The Freundlich coefficient K_f values (2.642 for WS500 *vs.* 2.335 for WS300), which were >1, indicating favorable adsorption and stronger affinity of WS500.[26] Notably, the Langmuir model achieved higher fitting accuracy (0.994 for WS300 and 0.998 for WS500) than the Freundlich model (0.955 for WS300 and 0.965 for WS500) (Table 1), demonstrating monolayer adsorption dominates the process.[27]

To further evaluate the adsorption performance of WS500, its maximum adsorption capacity was compared with those of other biochar-based adsorbents reported in the literature. Upon comparison, the q_m value of WS500 for Cr(VI) is at a moderate level among unmodified biochars derived from agricultural wastes.[28–31] Given the wide availability of wheat straw feedstock and the facile, low-energy preparation process, WS500 can be considered a promising and cost-effective adsorbent for Cr(VI) removal from aqueous environments.

3.2 Adsorption kinetics model

Fig. 2a and b present the adsorption kinetic curves of Cr(VI) onto WS300 and WS500. During the initial adsorption phase (the first 2 h), the adsorption capacity of both biochars increased rapidly, with WS500 exhibiting a steeper slope than WS300. This sharp rise was attributed to the abundant available active sites on the surfaces of both biochars during this initial stage, which provided ample binding sites for Cr(VI), thus facilitating rapid

Table 1 Adsorption isotherm parameters of Cr(VI) adsorption on WS300 and WS500

	Langmuir model			Freundlich model		
Samples	q (mg g^{-1})	K_L (mg L^{-1})	R_L^2	n	K_f [(mg g^{-1})((mg L^{-1})$^{-1}$)$^{1/n}$]	R_f^2
WS300	12.07	0.026	0.994	2.337	2.335	0.955
WS500	23.39	0.045	0.998	2.570	2.642	0.965

surface adsorption. After 2 h, the adsorption rate gradually decelerated, and the system reached dynamic adsorption equilibrium within approximately 12 h. Notably, WS500 achieved a higher equilibrium adsorption capacity than WS300. This difference could be explained by the progressive depletion of Cr(VI) in the solution and the gradual occupation of active sites on the adsorbent surfaces until saturation was approached.[32]

The kinetic fitting results (Fig. 2 and Table 2) demonstrated that the pseudo-second-order (PSO) model yielded higher R^2 values (0.992 for WS300; 0.991 for WS500) compared to the pseudo-first-order (PFO) model, and its calculated q_e values (8.67 and 10.78 mg g^{-1}) were in closer agreement with the experimental data. The PSO model assumes that the adsorption rate is governed by chemisorption, which involves valence forces between the adsorbent and adsorbate through electron sharing or exchange.[33] However, the PSO model is empirical in nature, and its fitting results should only be considered as a reference for the possibility that chemisorption may be the rate-controlling step. Further confirmation requires integration with additional characterization analyses.

For the intraparticle diffusion model (Fig. 2c and Table 3): stage 1 involves liquid film diffusion, stage 2 intraparticle diffusion/adsorption, and stage 3 equilibrium.[34] Non-zero intercepts in Table 3 indicated that intraparticle diffusion was not the sole rate-limiting step. The higher K_{d1} values than K_{d2} (0.747 > 0.13 for WS300; 0.835 > 0.19 for WS500) confirmed faster liquid film diffusion relative to intraparticle diffusion.[35]

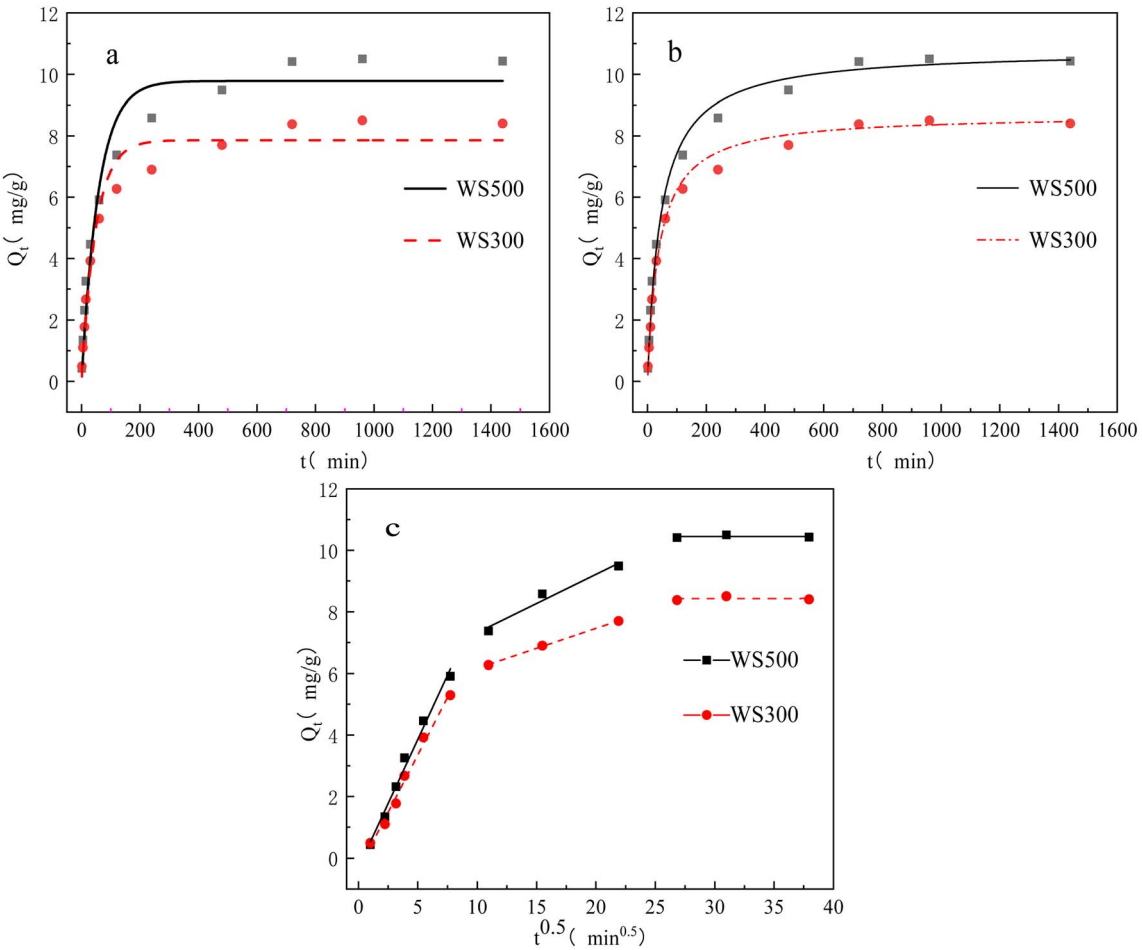

Fig. 2 Fitting results of the adsorption kinetic models: (a) PFO model; (b) PSO model; (c) intraparticle diffusion model.

Table 2 Fitting parameters of the dynamic model

	PFO model			PSO model		
Samples	q_e (mg g^{-1})	K_1 (min^{-1})	R_1^2	q_e (mg g^{-1})	K_2 (g (mg min)$^{-1}$)	R_2^2
WS300	7.86	0.003	0.962	8.67	0.002	0.992
WS500	9.78	0.017	0.955	10.78	0.002	0.991

Table 3 Fitting parameters of the intraparticle diffusion model

Samples	K_{d1}	K_{d2}	K_{d3}	C_1	C_2	C_3	R_1^2	R_2^2
WS300	0.747	0.13	1.78×10^{-4}	−0.386	4.861	8.422	0.987	0.999
WS500	0.835	0.19	4.44×10^{-5}	−0.317	5.424	10.447	0.983	0.935

Table 4 The characteristic parameters of wheat straw biochar prepared at various pyrolysis temperatures

	Elemental mass ratio (%)					Atomic molar ratio			
Samples	C	H	N	S	O	H/C	O/C	(N + O)/C	Ash mass content (%)
WS300	57.10	4.21	2.14	0.40	36.15	0.074	0.632	0.670	10.6
WS500	79.39	4.10	3.05	0.33	13.13	0.052	0.168	0.204	31.6

Critically, WS500 exhibited greater K_d values in stages 1–2 (0.835 *vs.* 0.747; 0.19 *vs.* 0.13), indicating that WS500 exhibited faster adsorption rate. This may be attributed to the provision of more available adsorption sites on WS500.

3.3 Elemental and thermogravimetric analyses

The organic element composition and ash content of wheat straw biochars prepared at various pyrolysis temperatures are presented in Table 4. As the pyrolysis temperature increased, the mass content of carbon (C) rose from 57.10% to 79.39%, while the oxygen (O) content decreased from 36.15% to 13.13%. The contents of N, H, and S remained relatively constant. The H/C atomic molar ratio declined from 0.074 for WS300 to 0.052 for WS500, indicating an enhanced aromatic condensation degree in WS500. Additionally, the O/C atomic molar ratio decreased from 0.632 to 0.168, signifying a reduced oxidation degree in the higher-temperature biochar. The (N + O)/C atomic molar ratio decreased significantly from 0.670 to 0.204, implying that WS500 possesses lower polarity and higher hydrophobicity than WS300.

To investigate the pyrolysis behavior and thermal stability of wheat straw under an N_2 atmosphere, thermogravimetric analysis was performed, and the resulting thermogravimetric (TG) and derivative thermogravimetric (DTG) curves are presented in Fig. 3. The pyrolysis process of wheat straw can be divided into three distinct stages. The first stage (30–200 °C) corresponds to the drying and dehydration phase. In this stage, the TG curve exhibits a gradual decline, with a cumulative mass loss of approximately 5% to 10%, primarily attributed to the evaporation of free and bound water in the raw wheat straw sample.[36] The second stage (200–450 °C) represents the pyrolysis stage and constitutes the core phase of thermal decomposition. Within this temperature range, the TG curve shows a sharp decline, with a mass loss accounting for approximately 70% to 80% of the total mass loss. A sharp characteristic peak appears in the DTG curve, with a peak temperature ranging from 300 °C to 400 °C, indicating the maximum mass loss rate throughout the entire pyrolysis process. During this stage, hemicellulose and cellulose undergo extensive pyrolytic decomposition, generating substantial amounts of volatile gases (*e.g.*, CO, CO_2, methane, aldehydes, and ketones) and tar.[37,38] The third stage (450–800 °C) is associated with the carbonization stage. As the temperature exceeds 450 °C, the TG curve gradually flattens, and the rate of mass loss

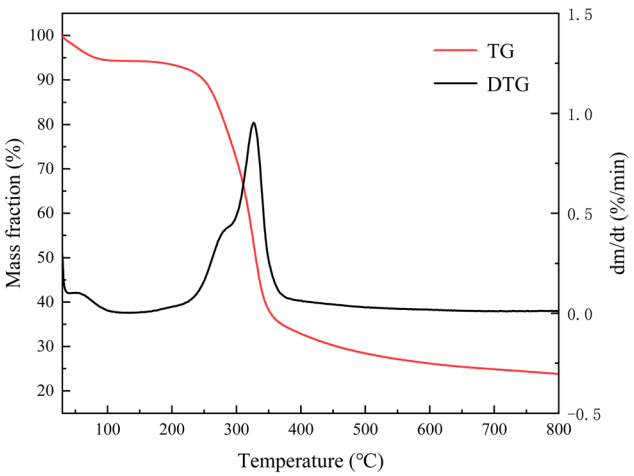

Fig. 3 Thermogravimetric (TG) and derivative thermogravimetric (DTG) curves of wheat straw obtained from 30 °C to 800 °C under a N_2 atmosphere.

Table 5 Specific surface area, pore volume, average pore diameter and zeta potential (pH = 6.0) of wheat straw, WS300, and WS500

Samples	Specific surface area ($m^2\ g^{-1}$)	Pore volume ($cm^3\ g^{-1}$)	Average pore diameter (nm)	Zeta potential (mV)
Wheat straw	4.7315	0.007	6.3405	—
WS300	0.2723	0.861	36.6197	−34.21
WS500	2.7165	1.020	38.1201	−31.15

decreases markedly. By 800 °C, the pyrolysis process is essentially complete, the sample mass remains stable, and the final carbon residue is approximately 20% to 30%.

3.4 BET and zeta potential analysis

The pore structures of raw wheat straw and its derived biochars were characterized *via* N_2 adsorption–desorption isotherms measured at −196 °C. As shown in Table 5, the specific surface area (SSA) was 0.2723 $m^2\ g^{-1}$ for WS300 and 2.7165 $m^2\ g^{-1}$ for WS500, while that of the raw wheat straw was 4.7315 $m^2\ g^{-1}$. The total pore volume of WS500 reached 1.02 $cm^3\ g^{-1}$, corresponding to an approximately 18.5% increase relative to WS300 (0.861 $cm^3\ g^{-1}$), and both values were substantially higher than that of the raw wheat straw (0.007 $cm^3\ g^{-1}$). Given that the pore volume data were derived from robust adsorption signals in the high-pressure region ($P/P_0 \approx 0.99$) and exhibited high measurement reproducibility,[39] this increase reliably reflects a substantial enhancement in porosity during high-temperature pyrolysis. Moreover, the average pore diameters of the two biochars (36.6 nm for WS300 and 38.1 nm for WS500) were notably larger than that of the raw wheat straw (6.34 nm). The comparable average pore diameters between the two biochars demonstrate that pyrolysis temperature imposed no significant effect on the characteristic pore dimensions.

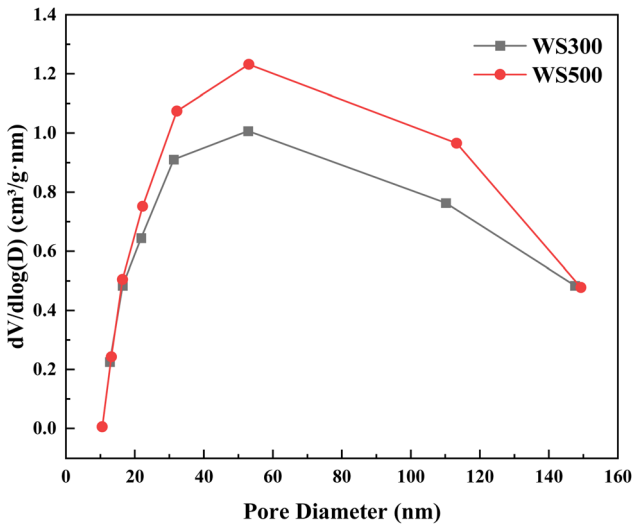

Fig. 4 The pore size distribution curves of WS300 and WS500 determined by the Barrett–Joyner–Halenda (BJH) method. Both biochars exhibit similar distribution patterns; WS500 displays higher pore volumes than WS300 across the measured range.

Fig. 4 presents the pore size distribution curves for both samples obtained using the Barrett–Joyner–Halenda (BJH) method. WS300 and WS500 exhibited similar distribution patterns, both showing pronounced peaks around 52 nm, indicating consistent pore architectures spanning the mesoporous to macroporous range (according to IUPAC pore classification). However, a key distinction lies in the consistently higher pore volume observed for WS500 across the entire measured pore size range, particularly between 20–140 nm. This overall elevation may suggest that elevated pyrolysis temperature contributed to an increase in pore number density rather than modifying the characteristic pore size.

In summary, despite the limited SSA values that constrain direct comparison *via* BET analysis, the marked increase in pore volume and the overall elevation of the pore size distribution collectively confirm that WS500 possesses a more developed porous network. From a structural standpoint, this makes WS500 more advantageous than WS300 as an adsorbent, as it can theoretically provide greater adsorption accommodation capacity and a higher density of accessible active sites.

The zeta potentials of the two biochars were measured at pH 6.0, and the results are shown in Table 5. At this pH, both biochars were negatively charged, with zeta potentials of −34.21 mV for WS300 and −31.15 mV for WS500. At this pH, Cr(VI) predominantly exists as anionic species, primarily $HCrO_4^-$ and CrO_4^{2-},[40] creating an electrostatic barrier to their approach toward the negatively charged biochar surfaces. Nevertheless, the substantial Cr(VI) uptake, especially by WS500, indicates that the adsorption process itself surpasses the electrostatic repulsion.

3.5 SEM-EDS analysis

The results of SEM imaging analysis of the biochar samples are presented in Fig. 5, and the EDS elemental mapping results for WS300-Cr and WS500-Cr are shown in Fig. 6 and 7, respectively. The wheat straw biochars exhibited a porous tubular morphology, which is potentially favorable for Cr(VI) adsorption. Elevating the pyrolysis temperature from 300 °C (Fig. 5a) to 500 °C (Fig. 5b) resulted in a marked increase in both pore quantity and volume within the biochar structure. These morphological observations were consistent with the pore volume and pore size distribution data presented in Table 5.

The EDS elemental mapping for C (Fig. 6b and 7b) confirmed the carbon-rich nature of the biochars. For WS300, the elemental mapping revealed strong spatial overlap between the distributions of silicon (Si, Fig. 6c) and oxygen (O, Fig. 6e). Furthermore, the distribution patterns of Si (Fig. 7c), aluminum

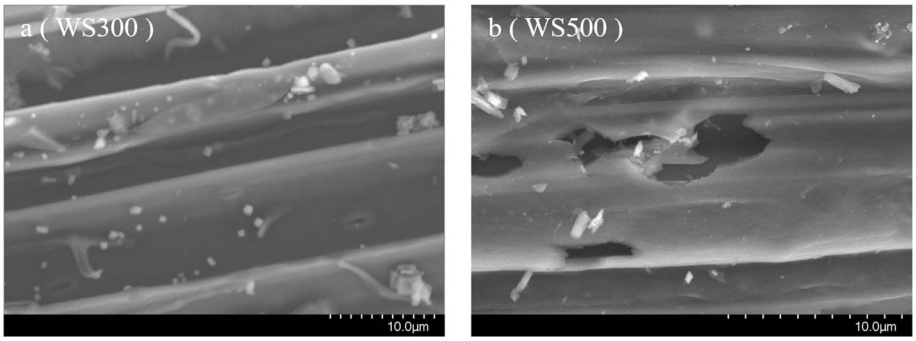

Fig. 5 SEM images of WS300 (a) and WS500 (b). Both biochars exhibit porous tubular structures; WS500 shows increased pore quantity and volume compared to WS300.

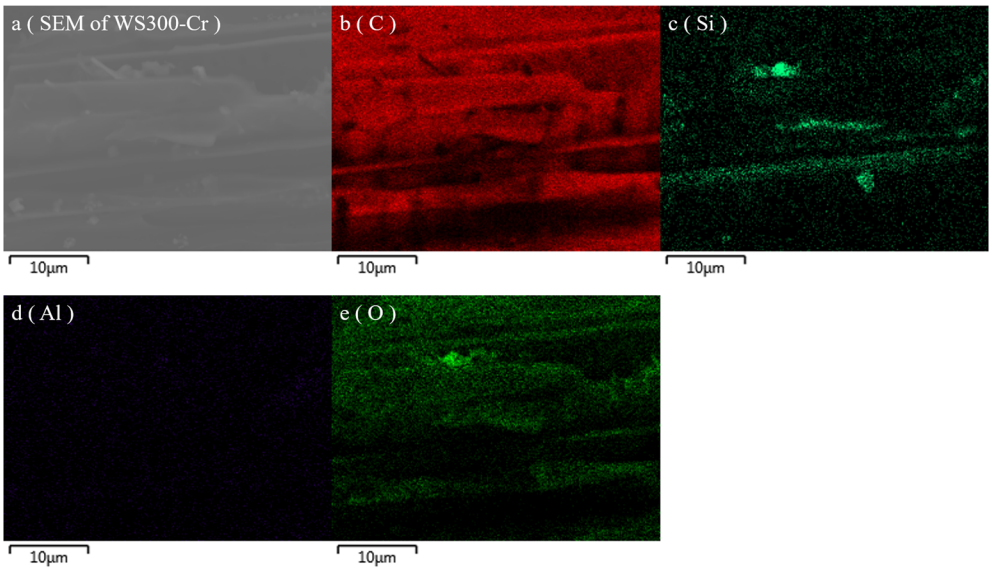

Fig. 6 SEM image (a) and corresponding EDS elemental mapping images (b–e) of WS300-Cr.

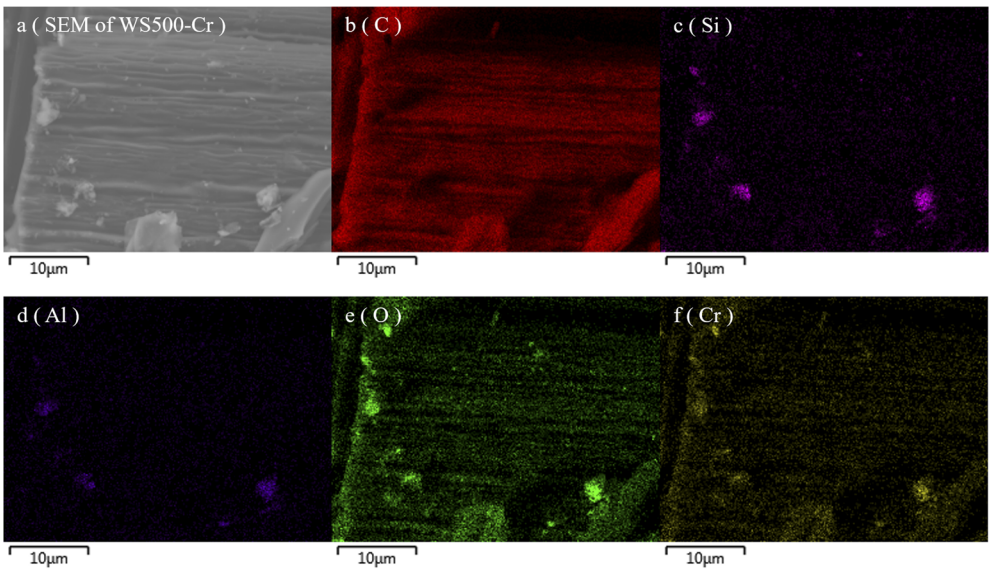

Fig. 7 SEM image (a) and corresponding EDS elemental mapping images (b–f) of WS500-Cr.

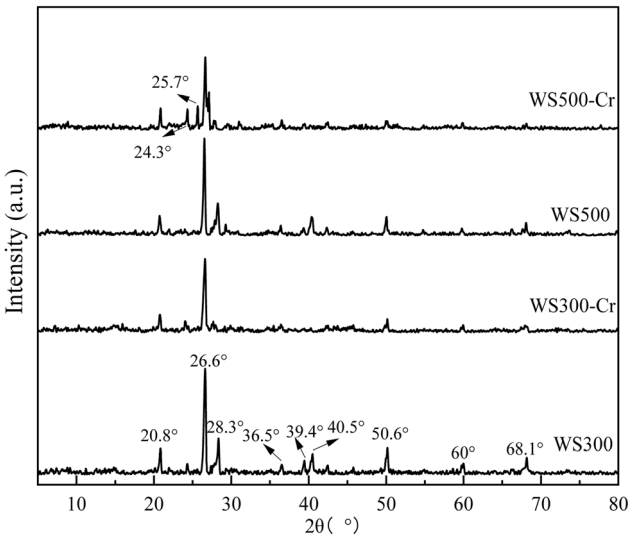

Fig. 8 X-ray diffraction patterns of wheat straw biochars (WS300 and WS500) before and after Cr(VI) adsorption. Both pristine biochars display multiple sharp diffraction peaks. After adsorption, a universal attenuation of all diffraction peak intensities is observed in both WS300-Cr and WS500-Cr, with some peaks showing near-complete disappearance.

(Al, Fig. 7d), and O (Fig. 7e) on the WS500 surface exhibited substantial spatial overlap. From the SEM image (Fig. 5), it is evident that the small particles dispersed on the biochar surfaces primarily comprise mineral components containing Si, Al, and O, such as silicates and aluminosilicates.

The EDS analysis of WS300-Cr and WS500-Cr samples (post Cr(VI) adsorption) demonstrated contrasting results. Specifically, WS300-Cr did not exhibit a significant Cr signal following adsorption, whereas a relatively prominent Cr signal was observed for WS500-Cr (Fig. 7f). This finding underscores the superior Cr(VI) removal capacity of WS500 compared to WS300. The distribution patterns of O and Cr on the WS500-Cr surface were highly consistent (Fig. 7e and f), suggesting that chromium was deposited in association with oxygen. This co-localization implies that some adsorbed Cr(VI) may have existed as oxyanions (*e.g.*, $HCrO_4^-$), while another portion is reduced to Cr(III), forming amorphous hydroxides (*e.g.*, $Cr(OH)_3$) or surface complexes, thereby leading to the observed Cr–O spatial correlation.[41] The absence of a distinct Cr signal by EDS for WS300-Cr, despite its lower adsorption capacity confirmed later by XPS, may be attributed to detection sensitivity limitations or the nature of the adsorbed species.

3.6 X-ray diffraction analysis

As illustrated in Fig. 8, the diffraction peaks observed at 20.8°, 26.6°, 36.5°, 50.6°, and 60.0° for both WS300 and WS500 corresponded to α-quartz. Peaks at 28.3°, 39.4°, 40.5°, and 68.1° were indicative of potassium salts, including KCl and K_2CO_3. Potassium was derived from the alkali metals inherent in the wheat straw,[42] primarily existing in ionic form within the organic matrix of the biomass.[43] During pyrolysis, the decomposition of the organic components released potassium, which subsequently combined with Cl^- and CO_3^{2-} to form crystalline potassium salts.[44] The broad diffraction feature observed between 20.8° and 26.0° suggested the presence of residual carbonaceous structures derived from cellulose/hemicellulose.[45]

A universal attenuation of XRD peak intensities was observed for the Cr(VI)-adsorbed biochars (WS300-Cr and WS500-Cr). This attenuation arose from the following mechanisms: (1) dissolution of soluble minerals during post-adsorption washing, particularly affecting KCl and K_2CO_3, as evidenced by the near-disappearance of their characteristic peaks, consistent with the high solubility of these potassium salts; (2) surface amorphization induced by newly formed non-crystalline chromium species (*e.g.*, Cr(III)-containing complexes or hydroxides), which may have reduced X-ray penetration efficiency or introduced disorder. This surface layer contributed to the uniform attenuation observed for quartz peaks. The presence and transformation of these mineral components have important implications for chromium immobilization. Although potassium salts themselves are not reducing agents, their dissolution may locally alter the surface micro-environment (*e.g.*, ionic strength or pH), thereby affecting Cr(VI) adsorption. The inhibitory effect of potassium salts on Cr(VI) adsorption was confirmed by background ion interference experiments (Fig. S1). Additionally, the attenuation of mineral reflections, together with the spatial co-localization of elements observed *via* EDS, suggests that mineral components served as substrates for the deposition or complexation of reduced Cr(III) species.

3.7 Fourier transform infrared spectrum analysis

Fourier-transform infrared spectroscopy was employed to characterize the surface functional group composition of the biochar samples. Fig. 9 presents comparative spectral profiles obtained before and after Cr(VI) adsorption. Broad bands centered around 3413 cm^{-1} were assigned to O–H stretching vibrations.[46] Peaks at approximately 1617 cm^{-1} (WS300) and 1624 cm^{-1} (WS500) represented stretching vibrations of aromatic C=C rings.[47] The absorption band near 1402 cm^{-1} demonstrated asymmetric bending vibrations of C–H bonds. Multiple peaks within the 1030–1140 cm^{-1} range (specifically at 1030 cm^{-1}, 1067 cm^{-1}, 1120 cm^{-1}, and 1140 cm^{-1}) arose from C–O–C stretching vibrations in ester, ether, and phenol groups.[34,48] Additional spectral features included a band at 949 cm^{-1} potentially associated with O–H bending vibrations or other functionalities, and out-of-plane C–H bending vibrations of aromatic systems observed at 615 cm^{-1}, 617 cm^{-1}, and 761 cm^{-1}.[48,49] Notably, the peaks around 615–617 cm^{-1} may also originate from metal–oxygen vibrations (*e.g.*, Cr–O), particularly in Cr-laden samples.[50] This spectral evidence confirms the presence of diverse oxygen-containing functional groups (hydroxyl, carboxyl, ester, ether) on the biochar surface.

A comparative analysis of the FTIR spectra of WS300 and WS500 revealed distinct differences in functional group composition. The O–H stretching vibration band (~3413–3415 cm^{-1}) exhibited significantly higher intensity in WS500

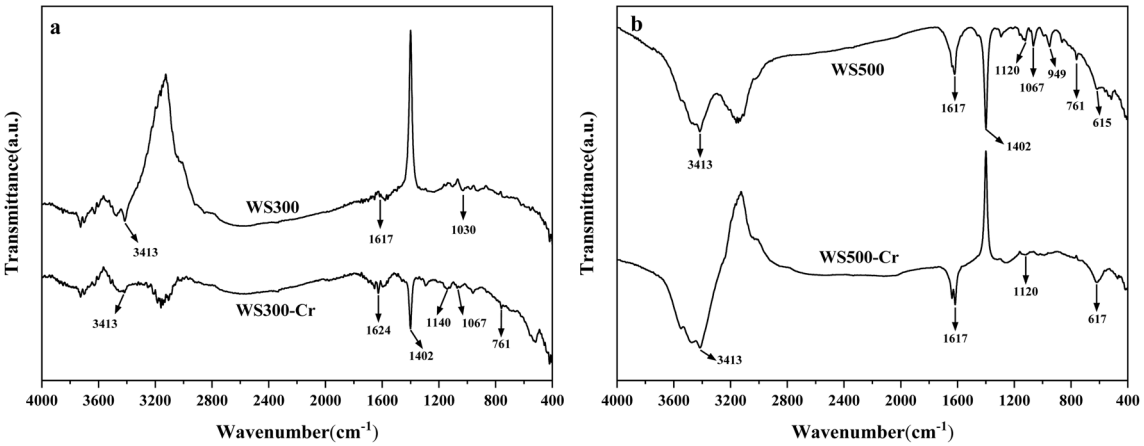

Fig. 9 FTIR spectra of wheat straw biochars (a) WS300 and (b) WS500 before and after Cr(VI) adsorption. WS500 exhibits stronger absorption intensities than WS300. After adsorption, intensity changes occur in both biochars; WS500 additionally shows band position shifts in the low-wavenumber region.

compared to WS300, suggesting a greater abundance of hydroxyl groups in the biochar pyrolyzed at 500 °C. The peak at 1617 cm^{-1}, associated with conjugated aromatic C=C vibrations, showed enhanced intensity in WS500 relative to WS300, indicating increased aromaticity at higher pyrolysis temperatures. In the region associated with C–O–C stretching vibrations (1000–1300 cm^{-1}), WS500 demonstrated stronger signals at 1067 cm^{-1} and 1120 cm^{-1} relative to the peak at 1030 cm^{-1} observed for WS300. Notably, a distinct characteristic peak at 949 cm^{-1} was observed in the spectrum of WS500, which was absent or extremely weak in that of WS300. Critically, after Cr(VI) adsorption, the characteristic peak at 615 cm^{-1} in pristine WS500 underwent a 2 cm^{-1} blue shift to 617 cm^{-1}, with a pronounced increase in absorption intensity, while no such spectral change was observed for WS300. This evolution correlates with Cr–O vibrations from newly formed Cr(III) surface complexes.

While elemental analysis indicated a lower bulk O/C ratio for WS500, suggesting a higher degree of carbonization and enhanced aromaticity, FTIR analysis revealed prominent absorption signals attributable to surface oxygen-containing functional groups on WS500. This phenomenon reveals the bulk-surface chemical heterogeneity of WS500: although its bulk phase is rich in aromatic carbon structures, its surface layer or pore edges retain or form abundant oxygen-containing functional groups, particularly hydroxyl and ether groups. These groups facilitate Cr(VI) reduction and subsequent Cr(III)–O complexation, potentially contributing to its superior Cr(VI) adsorption capacity compared to WS300.

3.8 X-ray photoelectron spectroscopy

Fig. 10a and b illustrate the XPS survey spectra of WS300 and WS500 before and after Cr(VI) adsorption. Prior to adsorption, distinct peaks corresponding to Si 2p (103.1 eV), C 1s (calibrated to 284.8 eV), N 1s (400.1 eV), and O 1s (532.7 eV) were observed for both biochars. Following Cr(VI) adsorption, a new peak emerged at 580.3 eV, attributable to Cr 2p in both materials.[51,52] Notably, while EDS analysis did not detect a significant Cr signal for WS300 post-adsorption, XPS confirmed Cr adsorption on WS300-Cr, albeit with lower intensity compared to WS500-Cr.

Fig. 10c presents the high-resolution Cr 2p spectra for WS300-Cr and WS500-Cr. The spectra exhibited characteristic spin–orbit doublets with Cr $2p_{3/2}$ at 577.6 eV and Cr $2p_{1/2}$ at 587.6 eV. Deconvolution of the Cr $2p_{3/2}$ region resolved two components: a dominant peak at 577.4 eV assigned to Cr(III) and a minor peak at 580.3 eV assigned to Cr(VI). Similarly, the Cr $2p_{1/2}$ region revealed a primary contribution from Cr(III) at 587.3 eV and residual Cr(VI) at 589.8 eV. This confirms the partial reduction of adsorbed Cr(VI) to Cr(III).[52] The reliability of this peak assignment was validated by a control XPS analysis of pure $K_2Cr_2O_7$, which showed no detectable Cr(III) signals under the same measurement conditions (Fig. S2). Additionally, diffuse reflectance spectroscopy (DRS) was attempted to characterize Cr species on the biochar surface after adsorption; however, no discernible signals were detected due to strong background absorption of the biochar matrix (Fig. S3). This reduction was further corroborated by aqueous chromium speciation analysis. In a representative adsorption experiment, 0.1 g of WS500 was used to adsorb 30 mL of Cr(VI) solution with an initial concentration of 20 mg L^{-1} (where initial total Cr was equal to Cr(VI)). After adsorption, the residual Cr(VI) concentration was 6.78 mg L^{-1}, while the residual total Cr concentration was 7.10 mg L^{-1}. The difference of 0.32 mg L^{-1} between total Cr and Cr(VI) indicated the presence of Cr(III) in the post-adsorption solution. This Cr(III) could have originated from the reduction of Cr(VI) by the biochar, providing independent evidence that reduction occurred during the adsorption process. Mass balance calculations further revealed that the amount of Cr(VI) removed from the solution (12.90 mg L^{-1}) substantially exceeded the total Cr remaining in solution, confirming that the majority of the reduced Cr(III) was simultaneously adsorbed onto the biochar surface. The more pronounced Cr(III) signals for WS500-Cr indicated its stronger

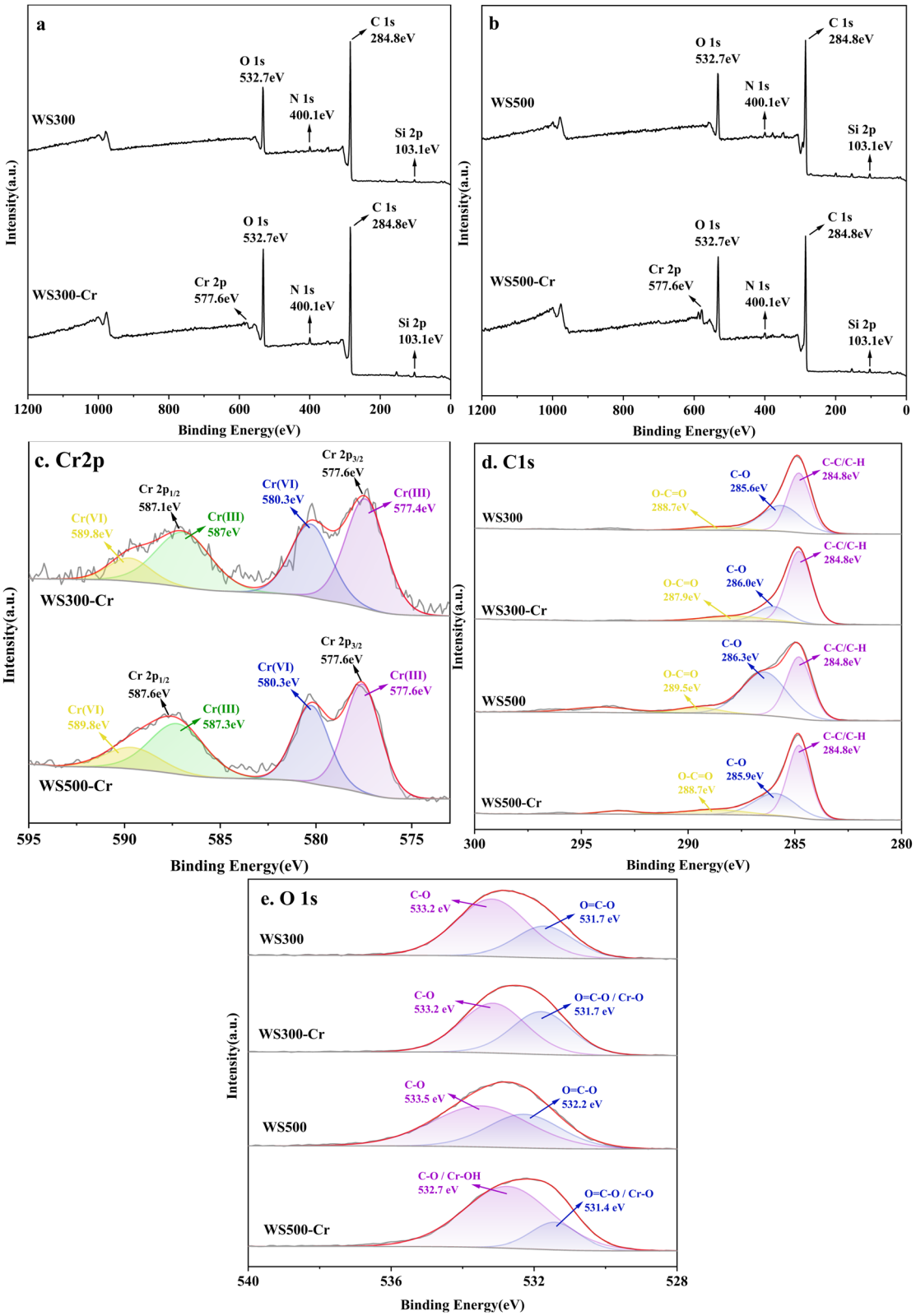

Fig. 10 XPS spectra of wheat straw biochars (WS300 and WS500) before and after Cr(VI) adsorption: (a and b) survey scans showing the appearance of chromium signals after adsorption; (c) Cr 2p high-resolution spectra of WS300-Cr and WS500-Cr showing peaks corresponding to both Cr(III) and Cr(VI); (d and e) C 1s and O 1s spectra displaying modifications in surface functional groups.

reduction capability, likely facilitated by its abundant phenolic –OH groups (acting as electron donors) and enhanced C–O–C moieties (potentially acting as electron transfer mediators),[53] as evidenced by the intensified FTIR vibrations. Furthermore, FTIR analysis revealed a significantly higher intensity of the aromatic C=C bond in WS500, suggesting that its enhanced reduction capability may also be associated with aromatic carbon structures. The enhanced aromatic carbon structures in biochar may provide additional electron donors for Cr(VI) reduction by hosting persistent free radicals.[54] However, this potential contribution requires further targeted investigation.

Fig. 10d illustrates the high-resolution C 1s spectra of WS300, WS500, WS300-Cr, and WS500-Cr. Prior to adsorption, the C 1s spectrum of WS300 was deconvoluted into three peaks: C–C/C–H at 284.8 eV (53.44%), C–OH/C–O–C at 285.6 eV (40.12%), and O–C=O at 288.7 eV (6.44%). For WS500, the corresponding peaks were C–C/C–H (284.8 eV, 40.98%), C–OH/C–O–C (286.4 eV, 52.51%), and O–C=O (289.5 eV, 6.51%).[51] The significantly higher relative abundance of C–OH/C–O–C groups in WS500 (52.51% *vs.* 40.12% in WS300) aligned with the FTIR observations, contributing to its superior affinity for Cr(VI).[55] After adsorption, the C 1s spectrum of WS300-Cr exhibited peaks at 284.8 eV (C–C/C–H, 69.59%), 286.0 eV (C–O, 18.25%), and 287.9 eV (O–C=O, 12.16%), while WS500-Cr showed peaks at 284.8 eV (C–C/C–H, 57.18%), 285.9 eV (C–O, 32.12%), and 288.7 eV (O–C=O, 10.70%). The marked reduction in C–OH/C–O–C content alongside the increase in O–C=O intensity confirmed the oxidation of C–OH groups to carboxyl moieties during the reduction of Cr(VI) to Cr(III).[56] Additionally, Cr(III) formed coordination bonds with oxygen-containing functional groups on the biochar surface (including pre-existing C–O and newly generated O–C=O), leading to the stabilization of Cr–O coordination complexes and subsequent immobilization.[57]

Fig. 10e depicts the high-resolution O 1s spectra before and after adsorption. Pre-adsorption analysis showed for WS300: O–C=O at 531.7 eV (31.09%) and C–OH at 533.2 eV (68.91%), while WS500 exhibited O–C=O at 532.2 eV (38.24%) and C–OH at 533.5 eV (61.76%).[51] Post-adsorption, WS300-Cr retained similar peaks at 531.7 eV (attributed to overlapping O–C=O and potential O–Cr contributions, 44.05%) and 533.2 eV (C–OH, 55.95%), consistent with its lower Cr adsorption capacity. In contrast, WS500-Cr displayed significant changes: a peak at 531.4 eV (assigned to O–C=O and O–Cr, 19.80%) showed an absolute decrease of 18.44% in the O–C=O component intensity compared to pre-adsorption, and a dominant new peak emerged at 532.7 eV (80.20%). This new peak at 532.7 eV was assigned to overlapping C–OH and Cr(III)–OH surface hydroxyl groups formed during the reduction and complexation process. The emergent Cr(III)–OH component (532.7 eV) directly correlated with the intensified Cr–O vibration observed at 617 cm^{-1} in FTIR spectra, providing complementary molecular-level evidence for Cr–O bonding. The pronounced decrease of pre-existing O–C=O groups and the emergence of the dominant Cr(III)–OH/C–OH peak at 532.7 eV provided direct evidence for Cr(III) complexation with surface oxygen functional groups. Crucially, the lack of characteristic diffraction patterns for crystalline chromium oxides (*e.g.*, Cr_2O_3 at 24.3° and 36.2°) in the XRD spectra of WS500-Cr (along with WS300-Cr) further verified that the immobilized chromium exists predominantly as atomically dispersed surface complexes or amorphous hydroxides rather than long-range ordered oxides.

Collectively, the XPS detection of Cr(III)–OH bonds, FTIR evidence of Cr–O vibrations, and XRD absence of crystalline Cr phases confirmed that chromium was immobilized through coordination with surface functional groups rather than through mineral precipitation, with EDS elemental colocalization further supporting this mechanism.

4 Conclusion

Pyrolysis temperature critically controlled wheat straw biochar properties and its Cr(VI) adsorption performance. Elevating temperature from 300 °C to 500 °C increased carbon content and pore volume while reducing polarity. Concurrently, higher pyrolysis temperature enriched redox-active functional groups (*e.g.*, phenolic –OH) and enhanced their electron-donating capacity. Consequently, WS500 achieved a 1.94-fold higher adsorption capacity than WS300. The process followed Langmuir monolayer adsorption and pseudo-second-order chemisorption, with mechanisms involving: (1) initial rapid uptake *via* pore filling; (2) Cr(VI) reduction to Cr(III) *via* electron transfer; (3) Cr(III) complexation.

Author contributions

He Jiajia: writing – original draft, writing – review & editing, visualization, formal analysis, methodology. Meng Bo: investigation, data curation. Qi Haiyang: validation, formal analysis. Fan Haoyu: investigation. Long Miao: investigation. Yu Mengjin: investigation. Bao Xianming: supervision, funding acquisition. Zhang Lichao: writing – original draft, writing – review & editing, project administration, resources, conceptualization, methodology.

Conflicts of interest

The authors declare that they have no known competing financial interests or personal relationships that could have appeared to influence the work reported in this paper.

Data availability

All data generated and analyzed during this study are included in this article.

The data supporting this article are available in the supplementary information (SI). Supplementary information: DPCI method for Cr(VI) concentration determination, background ion experiment, control XPS analysis of $K_2Cr_2O_7$, and DRS spectra. See DOI: https://doi.org/10.1039/d6ra00077k.

Acknowledgements

This work was supported by Key Foundation of Educational Commission of Anhui Province (2023AH050318 and

KJ2020A0040); the Innovation Team of Scientific Research Platform of Anhui Province, China (KJ2015TD001); Undergraduate Innovation and Entrepreneurship Training Program (S202510373141, S202410373017, S202410373062, 202410373006 and 202310373028).

References

1 D. A. Ali and R. G. Ali, Green synthesis of Carbonized Chitosan-Fe3O4-SiO2 nano-composite for adsorption of heavy metals from aqueous solutions, *BMC Chem.*, 2024, **18**(1), 147, DOI: 10.1186/s13065-024-01257-5.

2 P. J. Sheetal, Removal of lead ions from aqueous solution by modified nanocellulose, *Environ. Monit. Assess.*, 2024, **196**(6), 570, DOI: 10.1007/s10661-024-12742-8.

3 L. Rani, J. Kaushal and A. Lal Srivastav, Biochar as sustainable adsorbents for chromium ion removal from aqueous environment: a review, *Biomass Convers. Biorefin.*, 2024, **14**(5), 6083–6096, DOI: 10.1007/s13399-022-02784-8.

4 J. Chu, S. Xin, Y. He, *et al.*, Enhanced Adsorption of Hexavalent Chromium from Aqueous Solutions by Iron-manganese Modified Cedarwood Biochar: Synthesis, Performance, Mechanism, and Variables, *Bull. Environ. Contam. Toxicol.*, 2023, **111**(3), 43, DOI: 10.1007/s00128-023-03802-9.

5 V. Singh, N. Pant, R. K. Sharma, *et al.*, Adsorption studies of Pb (II) and Cd (II) heavy metal ions from aqueous solutions using a magnetic biochar composite material, *Separations*, 2023, **10**(7), 389, DOI: 10.3390/separations10070389.

6 Y. Chen, Q. Chen, H. Zhao, *et al.*, Wheat Straws and Corn Straws as Adsorbents for the Removal of Cr(VI) and Cr(III) from Aqueous Solution: Kinetics, Isotherm, and Mechanism, *ACS Omega*, 2020, **5**(11), 6003–6009, DOI: 10.1021/acsomega.9b04356.

7 L. D. Marsolla, G. M. Brito, J. C. C. Freitas, *et al.*, Sustainable enhancement of biochar and biochar composite properties through temperature-controlled pyrolysis of agricultural biomass and marble waste, *Waste Manage.*, 2025, **201**, 114799, DOI: 10.1016/j.wasman.2025.114799.

8 J. Cao, Y. Jiang, X. Tan, *et al.*, Sludge-based biochar preparation: pyrolysis and co-pyrolysis methods, improvements, and environmental applications, *Fuel*, 2024, **373**, 132265, DOI: 10.1016/j.fuel.2024.132265.

9 X. Shi, W. Yang, J. Li, *et al.*, The Application of Biochar as Heavy Metals Adsorbent: The Preparation, Mechanism, and Perspectives, *Int. J. Environ. Res.*, 2024, **18**(3), 41, DOI: 10.1007/s41742-024-00592-8.

10 X. Lu, X. Liu, W. Zhang, *et al.*, The residue from the acidic concentrated lithium bromide treated crop residue as biochar to remove Cr (VI), *Bioresour. Technol.*, 2020, **296**, 122348, DOI: 10.1016/j.biortech.2019.122348.

11 M. Irfan, F. Ishaq, D. Muhammad, *et al.*, Effect of wheat straw derived biochar on the bioavailability of Pb, Cd and Cr using maize as test crop, *J. Saudi Chem. Soc.*, 2021, **25**(5), 101232, DOI: 10.1016/j.jscs.2021.101232.

12 Z. Peng, X. Liu, H. Chen, *et al.*, Characterization of ultraviolet-modified biochar from different feedstocks for enhanced removal of hexavalent chromium from water, *Water Sci. Technol.*, 2019, **79**(9), 1705–1716, DOI: 10.2166/wst.2019.170.

13 U. Khalid and M. A. Inam, The Influence of Pyrolysis Temperature on the Performance of Cotton Stalk Biochar for Hexavalent Chromium Removal from Wastewater, *Water, Air, Soil Pollut.*, 2024, **235**(2), 114, DOI: 10.1007/s11270-024-06922-y.

14 S. Amita and A. Tripti, Effect of pyrolysis temperature on physicochemical properties and hexavalent chromium adsorption of the corncob biochars, *Biomass Convers. Biorefin.*, 2023, **13**(16), 15197–15210, DOI: 10.1007/s13399-023-05018-7.

15 J. Zuo, W. Li, Z. Xia, T. Zhao, C. Tan, Y. Wang and J. Li, Preparation of Modified Biochar and Its Adsorption of Cr(VI) in Aqueous Solution, *Coatings*, 2023, **13**, 1884, DOI: 10.3390/coatings13111884.

16 X. Zhang, X. Zhang and Z. Chen, Biosorption of Cr(VI) from aqueous solution by biochar derived from the leaf of Leersia hexandra Swartz, *Environ. Earth Sci.*, 2017, **76**, 67, DOI: 10.1007/s12665-016-6336-4.

17 Y. Li, X. Chen, L. Liu, *et al.*, Characteristics and adsorption of Cr(VI) of biochar pyrolyzed from landfill leachate sludge, *J. Anal. Appl. Pyrolysis*, 2022, **162**, 105449, DOI: 10.1016/j.jaap.2022.105449.

18 S. Singh, A. G. Anil, T. S. S. K. Naik, *et al.*, Mechanism and kinetics of Cr (VI) adsorption on biochar derived from Citrobacter freundii under different pyrolysis temperatures, *J. Water Process Eng.*, 2022, **47**, 102723, DOI: 10.1016/j.jwpe.2022.102723.

19 Y. Cai, J. Yang, Z. Ran, *et al.*, Optimizing Typha biochar with phosphoric acid modification and ferric chloride impregnation for hexavalent chromium remediation in water and soil, *Chemosphere*, 2024, **354**, 141739, DOI: 10.1016/j.chemosphere.2024.141739.

20 X. Zhang, L. Zhang and A. Li, Eucalyptus sawdust derived biochar generated by combining the hydrothermal carbonization and low concentration KOH modification for hexavalent chromium removal, *J. Environ. Manage.*, 2018, **206**, 989–998, DOI: 10.1016/j.jenvman.2017.11.079.

21 S. U. Gill, M. A. Inam, R. Iftikhar, *et al.*, Enhanced hexavalent chromium (VI) removal from water using nano zero valent iron modified orange peel powder biochar, *Int. J. Environ. Sci. Technol.*, 2025, **22**(13), 12599–12612, DOI: 10.1007/s13762-025-06381-w.

22 W. Stumm, *Aquatic Chemistry: Chemical Equilibria and Rates in Natural Waters*, Wiley, 3rd edn, 1996.

23 D. Mohan and C. U. Pittman, Activated carbons and low cost adsorbents for remediation of tri- and hexavalent chromium from water, *J. Hazard. Mater.*, 2006, **137**(2), 762–811, DOI: 10.1016/j.jhazmat.2006.06.060.

24 Y. Huang, S. Lin, P. Ai, *et al.*, Adsorption of Cr (VI) ions from wastewater using water-based polyacrylic resin, *Sci. Rep.*, 2025, **15**(1), 35645, DOI: 10.1038/s41598-025-19662-8.

25 D. Luo, L. Wang, H. Nan, *et al.*, Phosphorus adsorption by functionalized biochar: a review, *Environ. Chem. Lett.*, 2023, **21**(1), 497–524, DOI: 10.1007/s10311-022-01519-5.

26 X. S. Wang, L. F. Chen, F. Y. Li, *et al.*, Removal of Cr (VI) with wheat-residue derived black carbon: Reaction mechanism and adsorption performance, *J. Hazard. Mater.*, 2010, **175**(1/2/3), 816–822, DOI: 10.1016/j.jhazmat.2009.10.082.
27 J. Liao, T. Xiong, L. Ding, *et al.*, Design of a renewable hydroxyapatite-biocarbon composite for the removal of uranium (VI) with high-efficiency adsorption performance, *Biochar*, 2022, **4**(1), 29, DOI: 10.1007/s42773-022-00154-1.
28 A. Shakya, M. Vithanage and T. Agarwal, Influence of pyrolysis temperature on biochar properties and Cr (VI) adsorption from water with groundnut shell biochars: Mechanistic approach, *Environ. Res.*, 2022, **215**, 114243, DOI: 10.1016/j.envres.2022.114243.
29 A. Dahiya, A. Bhardwaj, A. Rani, *et al.*, Reduced and oxidized rice straw biochar for hexavalent chromium adsorption: Revisiting the mechanism of adsorption, *Heliyon*, 2023, **9**(11), 17, DOI: 10.1016/j.heliyon.2023.e21735.
30 J. Wan, F. Liu, G. Wang, *et al.*, Exploring different mechanisms of biochars in removing hexavalent chromium: Sorption, reduction and electron shuttle, *Bioresour. Technol.*, 2021, **337**(6), 125382, DOI: 10.1016/j.biortech.2021.125382.
31 Y. S. Shen, S. L. Wang, *et al.*, Removal of hexavalent Cr by coconut coir and derived chars – The effect of surface functionality, *Bioresour. Technol.*, 2012, **104**, 165–172, DOI: 10.1016/j.biortech.2011.10.096.
32 Y. Chen, S. Wang, Y. Li, *et al.*, Adsorption of Pb (II) by tourmaline-montmorillonite composite in aqueous phase, *J. Colloid Interface Sci.*, 2020, **575**, 367–376, DOI: 10.1016/j.jcis.2020.04.110.
33 Y. S. Ho and G. Mckay, Pseudo-second order model for sorption processes, *Process Biochem.*, 1999, **34**(5), 451–465, DOI: 10.1016/S0032-9592(98)00112-5.
34 N. Che, N. Liu, Y. Li, *et al.*, Three dimensional BC/rGA aerogel: preparation, characterization, and adsorption of Cr (VI), *Biochar*, 2022, **4**(1), 65, DOI: 10.1007/s42773-022-00191-w.
35 A. E. Nemr, Potential of pomegranate husk carbon for Cr(VI) removal from wastewater: kinetic and isotherm studies, *J. Hazard. Mater.*, 2009, **161**(1), 132–141, DOI: 10.1016/j.jhazmat.2008.03.093.
36 H. Yang, R. Yan, H. Chen, *et al.*, Characteristics of Hemicellulose, Cellulose and Lignin Pyrolysis, *Fuel*, 2007, **86**(12–13), 1781–1788, DOI: 10.1016/j.fuel.2006.12.013.
37 C. D. Blasi, Modeling chemical and physical processes of wood and biomass pyrolysis, *Prog. Energy Combust. Sci.*, 2008, **34**(1), 47–90, DOI: 10.1016/j.pecs.2006.12.001.
38 R. Li, K. Zeng, J. Soria, *et al.*, Product distribution from solar pyrolysis of agricultural and forestry biomass residues, *Renewable Energy*, 2016, **89**, 27–35, DOI: 10.1016/j.renene.2015.11.071.
39 M. Thommes, Physisorption of gases, with special reference to the evaluation of surface area and pore size distribution (IUPAC Technical Report), *Pure Appl. Chem.*, 2016, **87**(1), 25, DOI: 10.1515/pac-2014-1117.
40 J. Kota and Z. Stasicka, Chromium occurrence in the environment and methods of its speciation, *Environ. Pollut.*, 2000, **107**(3), 263–283, DOI: 10.1016/S0269-7491(99)00168-2.
41 M. Chigondo, B. Nyamunda, M. Maposa, *et al.*, Histidine-Functionalised Polypyrrole Hybrid Nanocomposite for Adsorption of Toxic Hexavalent Chromium from Water, *Water, Air, Soil Pollut.*, 2024, **235**(9), 572, DOI: 10.1007/s11270-024-07371-3.
42 X. Xiao, B. L. Chen and L. Z. Zhu, Transformation, morphology, and dissolution of silicon and carbon in rice straw-derived biochars under different pyrolytic temperatures, *Environ. Sci. Technol.*, 2014, **48**(6), 3411–3419, DOI: 10.1021/es405676h.
43 M. H. Martin and H. Marschner, *Mineral Nutrition of Higher Plants*, 1988.
44 J. H. Yuan, R. K. Xu and H. Zhang, The forms of alkalis in the biochar produced from crop residues at different temperatures, *Bioresour. Technol.*, 2011, **102**(3), 3488–3497, DOI: 10.1016/j.biortech.2010.11.018.
45 Y. Mukhambet, D. Shah, G. Tatkeyeva, *et al.*, Slow pyrolysis of flax straw biomass produced in Kazakhstan: Characterization of enhanced tar and high-quality biochar, *Fuel*, 2022, **324**(PartB), 124676, DOI: 10.1016/j.fuel.2022.124676.
46 X. N. Zhang, G. Y. Mao, Y. B. Jiao, *et al.*, Adsorption of anionic dye on magnesium hydroxide-coated pyrolytic biochar and reuse by microwave irradiation, *Int. J. Environ. Sci. Technol.*, 2014, **11**, 1439–1448, DOI: 10.1007/s13762-013-0338-5.
47 S. Ramola, T. Mishra, G. Rana, *et al.*, Characterization and pollutant removal efficiency of biochar derived from baggase, bamboo and tyre, *Environ. Monit. Assess.*, 2014, **186**, 9023–9039, DOI: 10.1007/s10661-014-4062-5.
48 S. B. A. Hamid, Z. Z. Chowdhury and S. M. Zain, Base catalytic approach: a promising technique for the activation of biochar for equilibrium sorption studies of copper, Cu (II) ions in single solute system, *Materials*, 2014, **7**(4), 2815–2832, DOI: 10.3390/ma7042815.
49 D. Özçimen and A. Ersoy-Meriçboyu, Characterization of biochar and bio-oil samples obtained from carbonization of various biomass materials, *Renewable energy*, 2010, **35**(6), 1319–1324, DOI: 10.1016/j.renene.2009.11.042.
50 S. Ibrahim, R. M. M. Morsi and S. M. Abo-Naf, Role of Mn/Cr dual-doped ZnO nanoparticles of diluted magnetic semiconductors: influence on structural and electrical properties, *Appl. Phys. A*, 2021, **127**(12), 1–8, DOI: 10.1007/s00339-021-05056-w.
51 H. Zhang, R. H. Li and Z. Q. Zhang, A versatile EDTA and chitosan bi-functionalized magnetic bamboo biochar for simultaneous removal of methyl orange and heavy metals from complex wastewater, *Environ. Pollut.*, 2022, **293**, 118517, DOI: 10.1016/j.envpol.2021.118517.
52 W. Q. Cai, Z. L. Li, J. H. Wei, *et al.*, Synthesis of peanut shell based magnetic activated carbon with excellent adsorption performance towards electroplating wastewater, *Chem. Eng. Res. Des.*, 2018, **140**, 23–32, DOI: 10.1016/j.cherd.2018.10.008.

53 Z. Y. Feng, N. Chen, C. P. Feng, *et al.*, Mechanisms of Cr(VI) removal by FeCl 3 -modified lotus stem-based biochar (FeCl 3 @LS-BC) using mass-balance and functional group expressions, *Colloids Surf., A*, 2018, **551**, 17–24, DOI: 10.1016/j.colsurfa.2018.04.054.

54 G. D. Fang, J. Gao, C. Liu, *et al.*, Key Role of Persistent Free Radicals in Hydrogen Peroxide Activation by Biochar: Implications to Organic Contaminant Degradation, *Environ. Sci. Technol.*, 2014, **48**(3), 1902–1910, DOI: 10.1021/es4048126.

55 N. H. Hsu, S. L. Wang, Y. H. Liao, *et al.*, Removal of hexavalent chromium from acidic aqueous solutions using rice straw-derived carbon, *J. Hazard. Mater.*, 2009, **171**(1/2/3), 1066–1070, DOI: 10.1016/j.jhazmat.2009.06.112.

56 X. Y. Xu, H. Huang, Y. Zhang, *et al.*, Biochar as both electron donor and electron shuttle for the reduction transformation of Cr(VI) during its sorption, *Environ. Pollut.*, 2019, **244**, 423–430, DOI: 10.1016/j.envpol.2018.10.068.

57 X. Dong, L. Q. Ma and Y. Li, Characteristics and mechanisms of hexavalent chromium removal by biochar from sugar beet tailing, *J. Hazard. Mater.*, 2011, **190**(1–3), 909–915, DOI: 10.1016/j.jhazmat.2011.04.008.